


















# DART Impact Ejecta Plume Evolution: Implications for Dimorphos

Andrew F. Cheng<sup>1</sup> , S. D. Raducan<sup>2</sup> , M. Jutzi<sup>2</sup>, T. L. Farnham<sup>3</sup> , E. Dotto<sup>4</sup>, V. Della Corte<sup>5</sup>, E. Mazzotta Epifani<sup>4</sup>, A. Rossi<sup>6</sup> , I. Gai<sup>7</sup>, J. Deshapriya<sup>4</sup>, P. Hasselmann<sup>4</sup> , I. Bertini<sup>8</sup>, A. Zinzi<sup>9</sup>, S. Ivanovski<sup>10</sup> , J. Brucato<sup>11</sup> , Giovanni Poggiali<sup>11</sup>, A. Lucchetti<sup>12</sup> , M. Pajola<sup>12</sup> , G. Zanotti<sup>13</sup>, M. Amoroso<sup>14</sup> , A. Capannolo<sup>13</sup> , G. Cremonese<sup>12</sup>, M. Dall'Ora<sup>15</sup> , S. Ieva<sup>4</sup> , G. Impresario<sup>14</sup>, M. Lavagna<sup>13</sup>, D. Modenini<sup>7</sup>, P. Palumbo<sup>8</sup> , D. Perna<sup>4</sup> , S. Pirrotta<sup>14</sup>, P. Tortora<sup>7</sup>, and M. Zannoni<sup>7</sup>

<sup>1</sup> Johns Hopkins University Applied Physics Laboratory, Laurel, MD 20723, USA; [andrew.cheng@jhuapl.edu](mailto:andrew.cheng@jhuapl.edu)

<sup>2</sup> Space Research and Planetary Sciences, Physikalisches Institut, Univ. of Bern, Bern, Switzerland

<sup>3</sup> Univ. of Maryland College Park, College Park, MD 20742, USA

<sup>4</sup> INAF-Osservatorio Astronomico di Roma, Via Frascati 33, I-00078 Monte Porzio Catone, Rome, Italy

<sup>5</sup> INAF-Istituto di Astrofisica e Planetologia Spaziale, Rome, Italy

<sup>6</sup> IFAC-CNR, Sesto Fiorentino, I-50019, Firenze, Italy

<sup>7</sup> Alma Mater Studiorum, University of Bologna, Forlì, Italy

<sup>8</sup> Università degli Studi di Napoli Parthenope, Napoli, Italy

<sup>9</sup> ASI Space Science Data Center, Via del Politecnico, I-00133, Rome, Italy

<sup>10</sup> INAF-Osservatorio Astronomico di Trieste, Trieste, Italy

<sup>11</sup> INAF-Osservatorio Astronomico di Arcetri, Firenze, Italy

<sup>12</sup> INAF-Osservatorio Astronomico di Padova, Vicolo Osservatorio 5, I-35122, Padova, Italy

<sup>13</sup> Politecnico di Milano, Milan, Italy

<sup>14</sup> ASI, Via del Politecnico, I-00133, Rome, Italy

<sup>15</sup> INAF-Osservatorio Astronomico di Capodimonte, Napoli, Italy

Received 2023 August 24; revised 2024 April 17; accepted 2024 April 18; published 2024 May 21

## Abstract

The NASA Double Asteroid Redirection Test (DART) spacecraft impacted the moon Dimorphos of the [65803] Didymos binary system and changed the binary orbit period, demonstrating asteroid deflection by a kinetic impact and indicating that more momentum was transferred to Dimorphos by escaping impact ejecta than was incident with DART. Images of the DART impact ejecta plume were obtained by the Light Italian cubesat for Imaging of Asteroids (LICIACube) in the first few minutes after the DART impact. The ejecta plume imaged by LICIACube 158 s after the DART impact prior to closest approach shows no evidence for plume clearing at low altitude. The ejecta plume imaged 175 s after the DART impact is optically thick up to projected altitudes of 200 m above the surface of Dimorphos. These observations are compared with models of the impact ejecta plume optical depth, structure, and evolution, which are developed from point-source scaling models fitted to numerical simulations of the DART impact into a rubble pile Dimorphos with different material strengths. The observations of the impact plume optical depth and the high momentum transfer from the DART impact are not consistent with impact and ejecta plume models assuming the Dimorphos cohesive strength to be as high as 5000 Pa. Models with 5 and 50 Pa Dimorphos cohesive strength provide the overall best consistency with plume opacity observations and high momentum transfer.

*Unified Astronomy Thesaurus concepts:* Asteroid satellites (2207); Asteroid surfaces (2209); Near-Earth objects (1092)

## 1. Introduction

The NASA Double Asteroid Redirection Test (DART) mission impacted the moon Dimorphos of the [65803] Didymos binary asteroid system (Daly et al. 2023) on 2022 September 26, changing the secondary's orbit by kinetic impact. Ground-based telescopic observations showed that the DART impact caused a reduction of the binary orbit period by  $33 \pm 1$  minutes (at  $3\sigma$ ; Thomas et al. 2023). The momentum transfer to Dimorphos from the DART impact was enhanced by a factor  $\beta$  over the momentum incident with DART in the direction of the net ejecta momentum (Cheng et al. 2023 and Appendix A), where  $\beta = 3.61^{+0.19}_{-0.25}(1\sigma)$  at the nominal Dimorphos density of  $2400 \text{ kg m}^{-3}$  (Daly et al. 2023). This  $\beta$  indicates that more momentum was transferred to Dimorphos

from escaping impact ejecta than was incident with DART (Cheng et al. 2023).

Light Italian cubesat for Imaging of Asteroids (LICIACube), a 6U cubesat contributed to DART by the Italian Space Agency (ASI), made a flyby of Didymos with the closest approach time delayed by 167 s from the DART impact in order to image the impact ejecta plume and study its evolution (Dotto et al. 2024). The ejecta plume structure, as imaged at a given time, is determined by the amount of ejecta that has reached the required distances from Dimorphos. Hence, the ejecta plume images can distinguish differences in plume structure and evolution resulting from different ejecta mass versus velocity distributions from targets of different strength and porosity (Cheng et al. 2020, 2022). LICIACube plume images can distinguish, for example, a porous target case with 4.4 kPa strength leading to a DART impact in the strength regime from a porous target case with a much lower 1 Pa strength for which the impact would have been in the gravity regime (Cheng et al. 2022). The different impact ejecta plume structures in the strength and gravity regimes are described by crater scaling



Original content from this work may be used under the terms of the [Creative Commons Attribution 4.0 licence](https://creativecommons.org/licenses/by/4.0/). Any further distribution of this work must maintain attribution to the author(s) and the title of the work, journal citation and DOI.

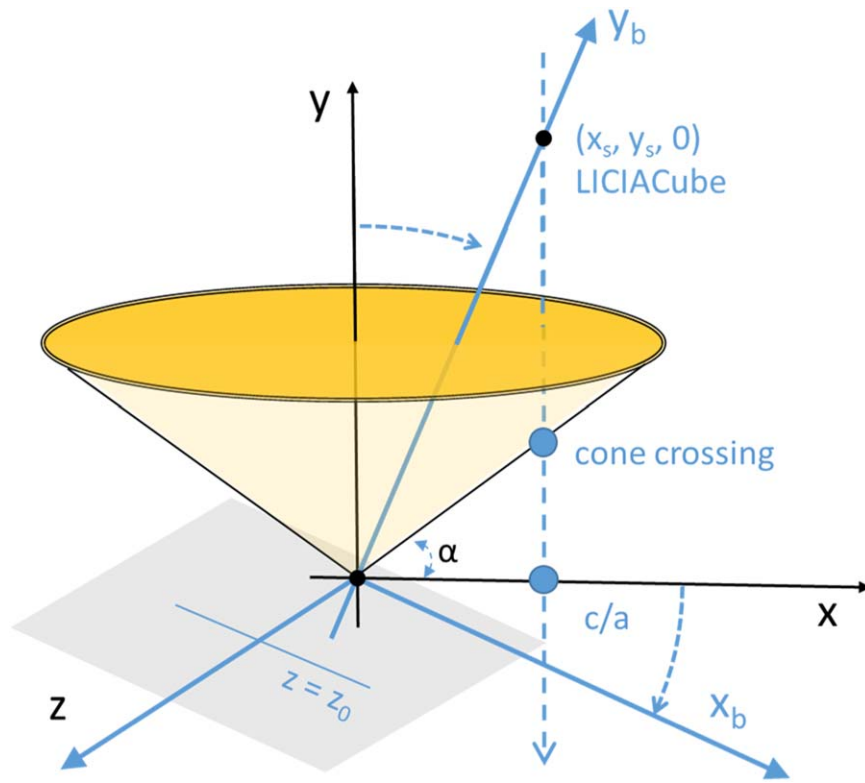


**Figure 1.** DART impact on Dimorphos is at the origin of Cartesian coordinates  $x$ - $y$ - $z$ . LICIACube trajectory is shown by the dashed blue line in the  $x$ - $y$  plane. The LICIACube position is  $(x_s, y_s, 0)$  in distant approach. The LOS from LICIACube to the Dimorphos impact site defines the  $y_b$  axis. The plane of sky at Dimorphos seen from LICIACube is the  $x_b$ - $z$  plane (shaded), which is rotated around  $z$  from  $x$ - $z$ . Optical depth profiles in the plane of sky calculated by Cheng et al. (2020) are at constant  $z = 0$ . Optical depth profiles at arbitrary  $z = z_0$  are given here. The DART impact ejecta cone, shown in yellow, is a hollow cone with negligibly thin walls. The cone axis is  $y$ , with ejecta angle  $\alpha$ . The ejecta cone crossing and closest approach indicated by  $c/a$  of the LICIACube trajectory are indicated by blue circles.

relations (Housen & Holsapple 2011; see Appendix B). In the strength regime, crater growth in late-stage evolution is arrested by target strength, and the observational signature of strength-regime cratering is the clearing of plume opacity immediately above the target surface, also described as ejecta plume detachment from the target surface. Hence, in the strength regime late-stage ejecta plume images show a plume detachment, but in the gravity regime such images would not display plume detachment.

The present work will apply the method of Cheng et al. (2022) to calculate ejecta plume optical depth profiles, using point-source scaling models of impact ejecta, for comparison with LICIACube plume images in order to characterize the ejecta mass versus velocity distribution and thereby constrain Dimorphos material properties, principally strength. This information is important, first because the DART measurements of the Didymos binary orbital period change from the DART impact (Thomas et al. 2023), and second because the corresponding momentum enhancement factor  $\beta$  (Cheng et al. 2023) did not determine the strength or the density of Dimorphos. Moreover, numerical simulations (Raducan & Jutzi 2022; Raducan et al. 2022) show that the DART impact can cause a global-scale deformation, or a reshaping of Dimorphos, if the strength of Dimorphos is low,  $\lesssim 10$  Pa, and the mass fraction of boulders is low,  $\lesssim 30\%$ . If the Dimorphos strength is higher,  $\gtrsim 10$  Pa, or if the mass fraction of boulders is higher,  $>30\%$ , then DART impact simulations predict formation of a crater (Raducan et al. 2022; Stickle et al. 2022).

The strength that is constrained in present work by ejecta plume imaging is the strength  $Y$  in point-source crater scaling

relations (see Appendix B) fitted to the ejecta mass versus velocity distributions calculated from numerical simulations of the DART impact into a rubble pile model of Dimorphos (Raducan et al. 2024). In these numerical simulations the strength is the cohesion (zero-pressure shear strength), which takes values 0–500 Pa in the matrix, while in the embedded boulders the strength and fracture model is such that tensile strength is  $\sim 10$  MPa.

## 2. DART Impact Ejecta Plume as Observed by LICIACube

The LICIACube flyby trajectory and the viewing geometry for plume images acquired by LICIACube are sketched in Figure 1. The ejecta plume optical depth along lines of sight (LOSs) from LICIACube is calculated by the method of Cheng et al. (2022). Orthogonal directions  $x_b$  and  $z$  are defined in the plane of sky at Dimorphos as seen from LICIACube (see Figure 1). The  $x_b$  axis points from the impact site to the intersection of the LICIACube trajectory with the plane of sky;  $y_b$  is also nearly parallel to the incident velocity direction of DART projected into the plane of sky (because the DART and LICIACube velocities are nearly parallel). The present work calculates plume optical depth profiles versus distance  $b$  along arbitrary image lines at fixed  $z = z_0$  (see Figure 1). The parameters  $z_0$  and  $b$  are projected distances in the plane of sky and directly convert to pixel distances as seen in LICIACube plume images.

Figure 1 shows the viewing geometry for plume imaging by LICIACube from its flyby trajectory, in distant approach. In the model of Cheng et al. (2022) and in the present model, the ejecta form a hollow cone, where the cone walls are considered to have negligible thickness. Placing ejecta trajectories on a

thin, hollow cone is a good approximation for the purpose of calculating plume optical depth versus projected distance from the impact site and versus time after the impact, neglecting complex fine structures in the plume (Dotto et al. 2024). The DART impact site is at the coordinate origin, and the DART incident direction, which is also the axis of the ejecta cone, defines the  $y$ -axis. LICIAcube is at position  $(x_s, y_s, 0)$  on a flyby trajectory in the  $x$ - $y$  plane such that  $x_s = 58$  km and  $y_s$  decreases with time. As sketched in Figure 1, if the cone is extended to infinity, above altitudes that may actually be reached by ejecta at the time of image acquisition, the intersection of the LICIAcube trajectory with the ejecta cone occurs at the point labeled “cone crossing.” That is, LICIAcube passes through the ejecta cone at cone crossing.

With LICIAcube on distant approach viewing Dimorphos (before closest approach, with range to target  $\gg 58$  km), the LOS is roughly along the plume axis at a solar phase angle near  $60^\circ$ . These approach images will be said to be obtained from inside the ejecta cone. In these approach images, each LOS through the plume intersects the cone once.

LICIAcube passes through cone crossing before it reaches closest approach at time 167.3 s after the DART impact, 58 km from Dimorphos. After cone crossing and near closest approach, LICIAcube images would be obtained from outside the cone, at close range looking nearly perpendicular to the plume axis. However, no such images were obtained, because LICIAcube tracked Didymos through closest approach, but Dimorphos and the ejecta plume moved outside the camera field of view  $\sim 161$  s after the DART impact, about 6 s before closest approach. The ejecta plume was not reacquired until  $\sim 175$  s after the impact, about 8 s after closest approach. LICIAcube did not obtain any plume images from outside the ejecta cone near closest approach.

After the ejecta plume was reacquired, the plume images obtained on departure show Dimorphos in front of and obscuring the lowest portion of the plume. That is, the impact site is behind the limb of Dimorphos, and only the plume portion above the limb is imaged. The distant departure images are again viewing roughly along the plume axis, but now at a solar phase angle of about  $120^\circ$  (Pajola et al. 2022).

### 2.1. Point-source Scaling Models of DART Impact

In previous work, the point-source scaling relations of Housen & Holsapple (2011) were used to make predictions of the DART impact ejecta plume optical depth versus distance from Dimorphos and time after impact (Cheng et al. 2020, 2022), in order to infer physical properties of Dimorphos from LICIAcube imaging of the ejecta plume. The point-source scaling relations were previously used by Cheng et al. (2016) to predict momentum transfer from the DART impact and to predict changes in the binary orbit period, eccentricity, and inclination. The point-source scaling relations were also used successfully to describe crater scaling for the SCI impact onto Ryugu (Jutzi et al. 2022).

The previous ejecta plume models (Cheng et al. 2020, 2022) used the point-source scaling relations of Housen & Holsapple (2011), which were fitted to measured ejecta mass and velocity distributions from laboratory impact experiments. However, all of the ejecta plume models considered by Cheng et al. (2022) predicted momentum enhancement factors  $\beta$  that were too low, inconsistent with the DART determination of  $\beta$  (Cheng et al. 2023). In the present work, new ejecta plume models are used,

with Housen & Holsapple (2011) impact scaling relations fitted to numerical simulations of the DART impact into a rubble pile Dimorphos (Raducan et al. 2024) that do reproduce the DART impact  $\beta$ . The Housen & Holsapple (2011) scaling relations and the scaling parameters derived from fitting to numerical simulations of Raducan et al. (2024) are summarized in Appendix B. The strength parameter  $Y$  in the impact scaling relations is assumed to be equal to the matrix cohesion in the simulation model, an assumption that holds well for low-cohesion granular targets: asteroid Ryugu cratered by the Small Carry-on Impactor (Jutzi et al. 2022) and sand with small boulders (Ormö et al. 2022). The assumption is not valid for higher-strength and higher-cohesion targets (Güldemeister et al. 2015; Prieur et al. 2017).

The Raducan et al. (2024) numerical simulations of the DART impact used the Bern smoothed particle hydrodynamics (SPH) shock physics code with a fast time integration scheme to describe late-stage evolution (Jutzi et al. 2022), by making a transition to model a material with low bulk modulus, after passage of the initial shock and when flow is low velocity only (at transition times of 0.5, 20, 500 s). This numerical approach with the fast time integration scheme was used to model successfully the Hayabusa 2 SCI impact on the asteroid Ryugu (Jutzi et al. 2022). The Bern SPH simulations of the DART impact used a rubble pile model of Dimorphos. In this rubble pile model, a boulder population is embedded within a matrix, where the boulder configuration is obtained as the result of a gravitational collapse calculated by an  $n$ -body dynamical simulation using `pkdgrav` (Richardson et al. 2000), for a boulder size distribution consistent with the measured size-frequency distribution on the surface of Dimorphos (Pajola et al. 2023). Some boulders are removed and replaced by a matrix, in order to vary the volume fraction occupied by boulders. Three boulders at the impact site are modeled explicitly, using the global digital terrain model from Daly et al. (2023). For the Bern SPH simulations used in the present work to determine point-source scaling relations for the DART impact, the rubble pile model of Dimorphos had a volume fraction of boulders of 30%, and the bulk density was  $2350 \text{ kg m}^{-3}$ . The boulders had 10 MPa tensile strength and microporosity 10%, while the matrix had cohesive strength in the range 0–500 Pa and porosity 45%. The coefficient of internal friction was  $f = 0.55$ . The Bern SPH numerical simulations and results are described by Raducan et al. (2024), and more information on the point-source scaling of the DART impact is given in Appendix B.

### 2.2. Ejecta Plume Optical Depth

The ejecta plume optical depth along LOSs from LICIAcube is calculated by the method of Cheng et al. (2022). The DART impact ejecta are modeled as moving from the impact point on the surface of a cone as sketched in Figure 1, within a small range of ejection angles  $\alpha$  measured to the target surface, that is, within the range  $(\alpha, \alpha + \delta\alpha)$ . The ejection angle  $\alpha = 25^\circ$ , so the cone opening angle is  $130^\circ$  full width, consistent with the Hubble Space Telescope (HST) measured opening angle  $125^\circ \pm 10^\circ$  (Li et al. 2023) and the LICIAcube observation  $140^\circ \pm 4^\circ$  (Deshapriya et al. 2023; Dotto et al. 2024). For ejecta imaged within a few kilometers of the impact site, ejecta are considered to be released on rectilinear trajectories at constant speed. If, at the time  $t$  relative to the DART impact time, the LOS for an image pixel intersects the ejecta cone at

radial distance  $r$  from the impact site, then those ejecta were released at velocity  $v=r/t$ . This approximation considers ejecta always to be released from the origin at the impact site and thereby neglects the size and depth of the impact excavation or deformation compared to the radial distance  $r$ . At the intersection of the LOS with the ejecta cone, the annular volume element is written as volume =  $2\pi r^2 \cos \alpha \delta r \delta \alpha$ , and the path length through the intersection is written as path =  $\gamma r \delta \alpha$ , where  $\gamma > 1$  accounts for obliquity. The ejecta mass within the annular volume element is mass in  $\delta r = \left| \frac{dM_{ej}(v)}{dr} \right| \delta r$ , which is found from numerical differentiation of the cumulative mass distribution  $M_{ej}(v)$ . An LOS integration gives the optical depth contribution from the intersection (Cheng et al. 2020, 2022)

$$\begin{aligned} \text{optical depth } \tau &= \frac{\left| \frac{dM_{ej}(v)}{dr} \right| \delta r \gamma r \delta \alpha}{2\pi r^2 \cos \alpha \delta r \delta \alpha} \left( \frac{\text{area}}{\text{mass}} \right) Q \\ &= \frac{\left| \frac{dM_{ej}(v)}{dr} \right| \gamma}{2\pi r \cos \alpha} \left( \frac{\text{area}}{\text{mass}} \right) Q, \end{aligned} \quad (1)$$

where the factor  $\left( \frac{\text{area}}{\text{mass}} \right)$  is the total geometric cross section per unit mass of ejecta. The factor  $Q$  is the scattering or extinction efficiency, relating the geometric cross-section area to the scattering or extinction cross section, respectively. Here we simply adopt an extinction efficiency  $Q = 2$  for ejecta particles large compared to the wavelength (Hansen & Travis 1974; Cheng et al. 2022). The obliquity  $\gamma$  is found using the normal vector to the ejecta cone at the intersection of the LOS with the cone (Cheng et al. 2022).

The total geometric cross section per unit mass  $\left( \frac{\text{area}}{\text{mass}} \right)$  is calculated from the ejecta particle size distribution. Previous work (Cheng et al. 2020, 2022) assumed an Itokawa size distribution (Mazrouei et al. 2014; Tancredi et al. 2015), but the present work adopts a broken power-law size distribution consistent with HST observations of the DART ejecta (Li et al. 2023). Namely, the differential number of particles is  $n(s) = n_0 s^{-3.9}$  in the diameter range from  $s_1 = 2$  m to  $s_2 = 0.001$  m, and it is  $n(s) = 3.981 \times 10^3 n_0 s^{-2.7}$  in the diameter range from  $s_2 = 0.001$  m to  $s_3 = 3 \times 10^{-5}$  m. The area of particles is  $A_d = \int_{s_3}^{s_1} ds \pi s^2 n(s)/4$ , and the volume is  $V_d = \int_{s_3}^{s_1} ds \pi s^3 n(s)/6$ , yielding  $\left( \frac{\text{area}}{\text{mass}} \right) = \frac{A_d}{\rho_g V_d} = 0.1007 \text{ m}^2 \text{ kg}^{-1}$  for an assumed particle density  $\rho_g = 3000 \text{ kg m}^{-3}$ .

### 3. LICIAcube LUKE Images of Ejecta Plume

This work will analyze LICIAcube plume images obtained by the LICIAcube Unit Key Explorer (LUKE) camera. The LUKE camera (Dotto et al. 2021) is a multispectral visible imager at  $f/5$  with an RGB Bayer pattern filter on the focal array. The instantaneous field of view is  $78 \mu\text{rad pixel}^{-1}$ , for a ground sampling distance of 4.5 m at 58 km range. The full image field of view is  $9^\circ 2' \times 4^\circ 9'$ .

Figure 2 shows the image `liciacube_luke_12_1664234222_00002_01`, acquired 158 s after the DART impact, written as  $T + 158$  s. This is the  $R$ -plane of the RGB LUKE image (Dotto et al. 2024). It is a 0.2 ms exposure obtained at a range to Dimorphos of 82 km from inside the ejecta cone. The pixel scale is  $6.4 \text{ m pixel}^{-1}$ . Figure 2 is annotated to show the  $\mathbf{b}$  and  $\mathbf{z}$  directions ( $\mathbf{b}$  is in the direction of  $\mathbf{x}_b$  in Figure 1). The DART

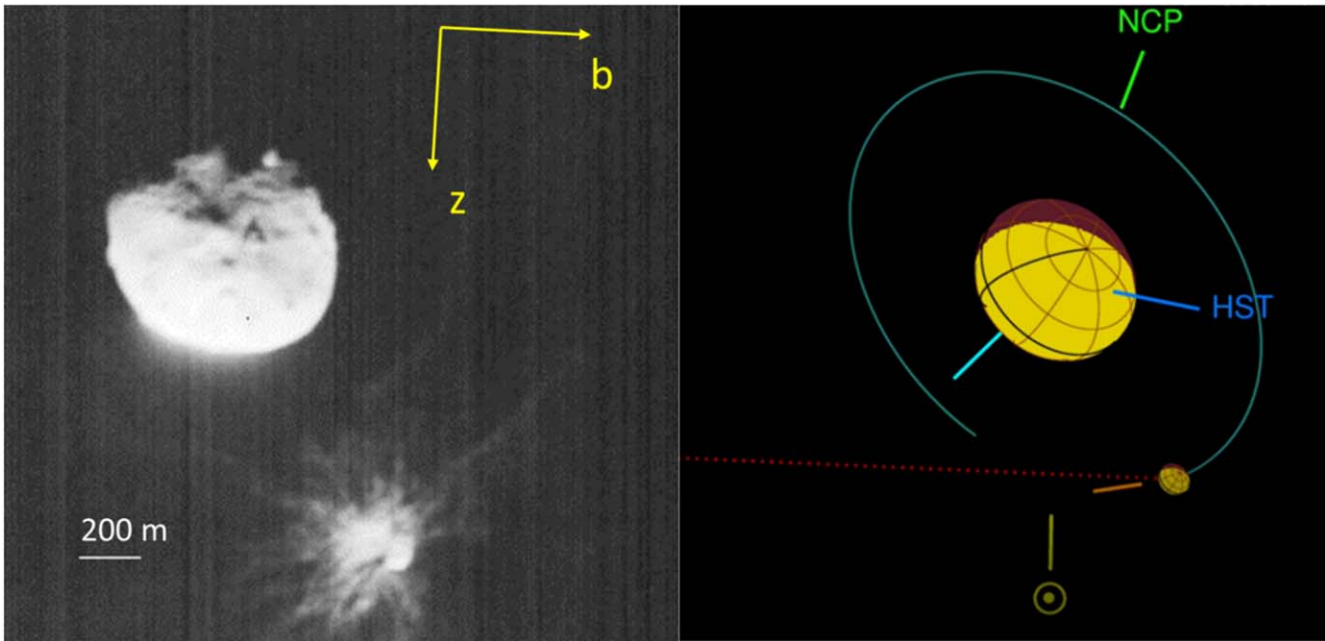
incident direction is  $44^\circ 8'$  from the image plane of sky (a vector from the impact site to DART points out of the page). The direction to the Sun is  $47^\circ 4'$  from the plane of sky (also out of the page), with the solar phase angle  $43^\circ 2'$ .

Figure 3 shows brightness profiles (labeled a–c) across the sunlit limb and the terminator on Didymos without the ejecta plume, for comparison with profiles across Dimorphos and the ejecta plume, where the ejecta plume is seen in front of the terminator and limb. In profile a, the steep rise and fall of brightness at the Didymos terminator and the sunlit limb, respectively, are contrasted with the more extended and gradually sloping brightness rise and fall in the corresponding profile d, indicating that the terminator and the sunlit limb of Dimorphos are not visible but are completely obscured by the optically thick ejecta plume. Likewise, comparison of profiles b and e shows a steep rise and fall of brightness at the terminator and limb of Didymos (profile b), versus a more gradually sloping brightness profile at Dimorphos (profile e), indicating that the limb and terminator are both completely obscured by an optically thick plume. Profile b above pixel distance 163 at Didymos shows evidence of an emission region (marked “glare”) near the subsolar point (Mazzotta Epifani et al. 2023), as well as the steep drop in brightness above pixel distance 158 at the sunlit limb at Didymos. Profile f at Dimorphos, above pixel distance 167, shows a similarly steep dropoff to those at the sunlit limb of Didymos in profiles b and c, indicating that the sunlit limb of Dimorphos is seen in profile f, partly obscured by ejecta above pixel distance 170.

The brightness profiles d–f in Figure 3 provide evidence that the ejecta plume is optically thick at low altitudes  $< 200$  m above Dimorphos. Additional evidence is found in the maximum brightness ( $\sim 0.7$  DN) seen in the ejecta plume (profiles d and e), which is similar to the peak brightness values seen on Didymos in profiles a–c, suggesting high optical thickness in the low-altitude ejecta plume. The highest Didymos brightness values, in profiles b and c near pixel distances 150–160, occur on sunward-facing slopes and are similar to the highest brightness values seen on Dimorphos (profile f, pixel distances 163–168).

Figure 3 provides further evidence for an optically thick plume in the form of plume shadow regions, which are shadowed from the Sun by more sunward plume material. A Z-shaped dark region is seen in the  $T+158$  s plume image, where the DART incident velocity direction (close to the ejecta cone axis) and the solar direction are such that the Z-shaped dark regions are shadowed by more sunward ejecta in the cone. Profile d encounters the Z-shaped plume shadow three times, causing sharp drops in brightness (near pixel distances 167, 175, and 181), and profile e encounters the plume shadow once near pixel distance 164. The appearance of the plume shadow region is similar to the shadow regions seen on Didymos caused by topographic features (e.g., in profile b near pixel distances 91 and 115).

Figure 4 shows the departure image `liciacube_luke_12_1664234239_01003_01` acquired at  $T+175$  s, with annotations to indicate the  $\mathbf{b}$  and  $\mathbf{z}$  directions ( $\mathbf{b}$  is in the direction of  $\mathbf{x}_b$  in Figure 1) and to show a 200 m scale bar at the distance of Dimorphos. Figure 4 shows the  $R$ -plane of the RGB LUKE image (Dotto et al. 2024). This was a short-exposure, 0.3 ms image acquired at a range to Dimorphos of 74.5 km, showing Dimorphos in front of the ejecta plume. The pixel scale is  $5.8 \text{ m pixel}^{-1}$ . In this image, the DART incident direction is



**Figure 2.** Left: LUKE image at  $T+158$  s, before closest approach. LICIACube is inside the ejecta cone. Didymos is the larger body at upper left, with Dimorphos and the ejecta plume at bottom. The scale bar at the distance of Dimorphos and directions of  $b$  and  $z$  axes are shown. Right: projected north celestial pole direction indicated by NCP. The solar illumination direction is indicated by the solar symbol (solar direction is  $47^\circ 4'$  out of the page). Viewing direction from HST is indicated by HST. The dotted red line is the DART incident trajectory (incident velocity vector directed  $44^\circ 8'$  into the page). The orbit of Dimorphos is shown in blue, as is positive rotation and orbital pole. The orange bar shows the direction of Dimorphos orbital motion.

$-38^\circ 2'$  from the plane of sky (direction to DART is into the page). The direction to the Sun is  $6^\circ$  from the plane of sky (out of page), with the solar phase angle  $85^\circ$ .

The  $T = 175$  s image in Figure 5 shows an annular dark region around Dimorphos, identified as a plume shadow (Dotto et al. 2024), where the low-altitude plume is shadowed by more sunward plume material. This shadowing is possible on the near side of the ejecta cone closer to LICIACube, with the solar direction only  $6^\circ$  out of the plane of sky and with the DART velocity  $38^\circ 2'$  outward from the sky plane. The dark annular region around Dimorphos cannot be an empty void region, because if it were empty, the other side of the ejecta cone (farther from LICIACube) should be visible and would appear bright. The same annular region was imaged only 17 s earlier at  $T+158$  s (in Figure 3), and optically thick plume material is seen there. With the annular region both shadowed and optically thick, it would appear dark as in the  $T+175$  image.

Figure 5 shows brightness profiles (labeled a–b) across the sunlit limb and the terminator on Didymos without the ejecta plume, for comparison with profiles (labeled c–d) across Dimorphos and the ejecta plume, with Dimorphos in front of, and partly obscuring, the ejecta plume. The profiles are oriented in the projected solar direction to study limb and terminator brightness. Profile a shows a steep rise and fall of brightness at the sunlit limb and the terminator of Didymos, respectively, along with sharp brightness dips in the shadow regions of craters. These features are compared with those in profile d through the ejecta plume (pixel distance  $< 60$ ), then the shadow around Dimorphos (pixel distance  $\sim 68$ ), and finally across the sunlit limb (pixel distance  $\sim 71$ ) and terminator (pixel distance  $\sim 81$ ) on Dimorphos. The steepness of the brightness drop entering the plume shadow (slope near pixel distance 64 in profile d) is similar to that seen for topographic shadows on Didymos (e.g., in profile a, near pixel distances 81 and 115). The plume shadowing indicates that the plume is optically

thick. The similar peak brightness of the ejecta plume and of Dimorphos in profile d also supports an optically thick plume. The brightness profile c indicates that the peak brightness seen in the plume (pixel distance  $\sim 112$ ) exceeds that seen on Dimorphos. Profile c, which is on the plume only, also crosses a plume terminator (pixel distance  $\sim 117$ ). This plume terminator is parallel to the Dimorphos terminator and is sharply defined up to  $\sim 200$  m from Dimorphos. It is inferred that the ejecta plume at  $T+175$  s is optically thick up to plane-of-sky distance  $\sim 200$  m from Dimorphos.

#### 4. Ejecta Plume Optical Depth Profiles

Figure 6 shows the DART impact ejecta mass–velocity distributions  $M(v)$  from point-source scaling for four target cases, in which the strength  $Y$  takes four values from 5 Pa to 5 kPa, with other scaling parameters and target properties held constant. The strength–gravity transition for the DART impact onto Dimorphos is at strength  $Y = 4$  Pa (Raducan et al. 2024; see also Appendix B). The DART impact is in the strength regime in all four cases, but the  $Y = 5$  Pa case is near the strength–gravity transition.

Figures 7 and 8 show extinction optical depth profiles of  $\tau$  versus the distance  $b$ , calculated for four positive values of  $z_0$ . The plume optical depth model is symmetric in  $\pm z$ , so that  $\tau(b, z_0) = \tau(b, -z_0)$ . The optical depth profiles are calculated using the point-source scaling  $M_{ej}(v)$  distributions of Figure 6.

Figure 7 shows optical depth profiles for the two low-strength target cases, 5 and 50 Pa, at the two image times  $T + 158$  s and  $T + 175$  s. In both target cases the DART impact would be in the strength regime, although the 5 Pa case is close to the strength–gravity transition. The profiles for the 5 and 50 Pa target cases are very similar, showing small decreases in  $\tau$ , on the order of 10%, going from 5 to 50 Pa strength, with larger decreases occurring closer to Dimorphos. This is

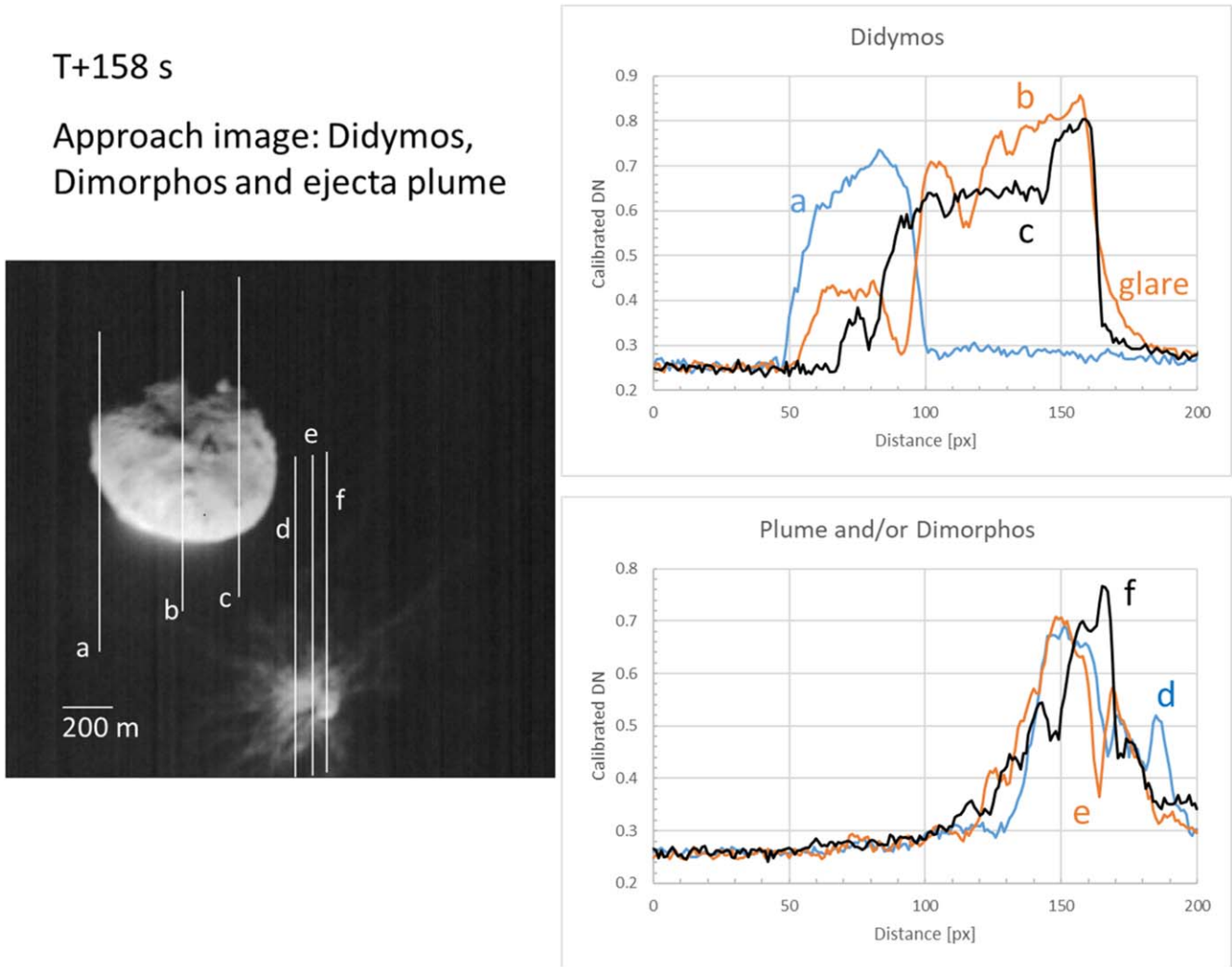


**Figure 3.** Brightness profiles across limbs and terminators of Dimorphos and Didymos, showing DN radiance in arbitrary units vs. pixel distance measured from top to bottom along image lines marked a–f. Profiles a–c are across the terminator (lower pixel distance) and sunlit limb (higher pixel distance) of Didymos, without ejecta plume. Profiles d–f are across the ejecta plume and/or Dimorphos. Dimorphos is partly obscured by the ejecta plume. Profile b above pixel distance 160 shows glare, indicating an excess emission region above the subsolar limb of Didymos. Profiles d and e pass through a Z-shaped plume shadow, in the T+158 s image, between pixel distances 160 and 180. The distance 200 m is 31 pixels.

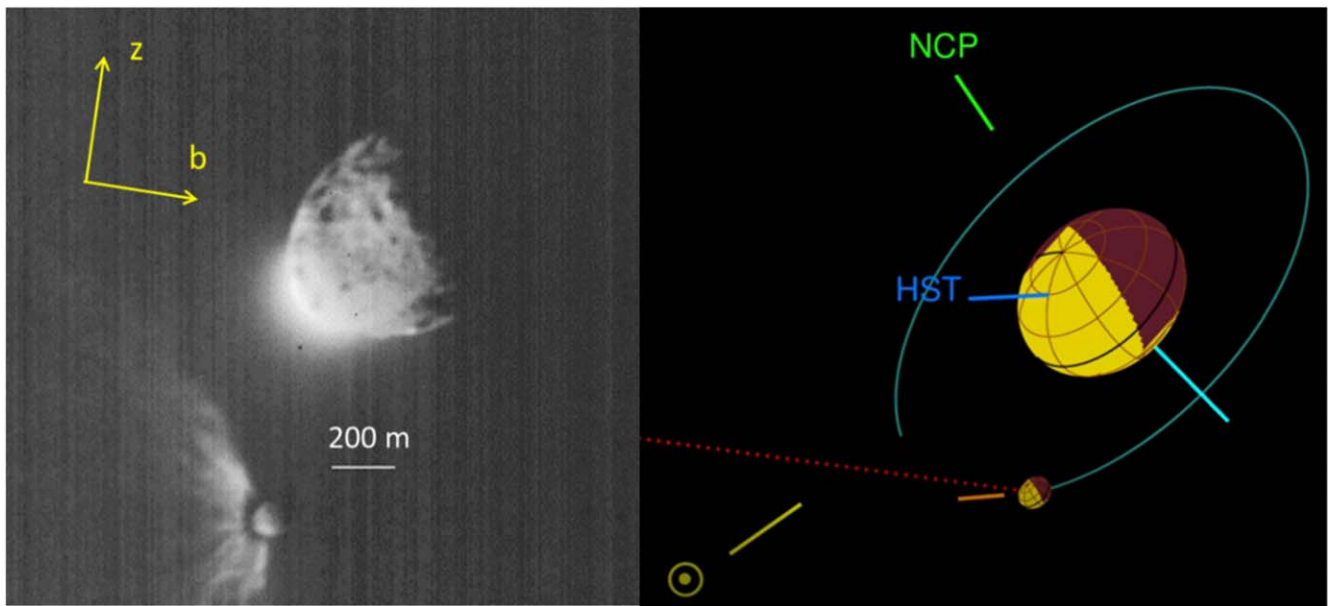
expected given the similar  $M_{ej}(v)$  in Figure 6 for the 5 and 50 Pa cases. There is only a subtle decrease in  $M_{ej}(v)$  at the lowest velocities going from 5 to 50 Pa. In both target cases, this decrease leads to small dips in the optical depth  $\tau$  occurring near the origin  $b = 0$  at T+175 s, but these small dips are not observable because Dimorphos is in front of the plume.

Figure 8 shows optical depth profiles for the two higher-strength target cases, 500 and 5000 Pa, at the two image times T+158 s and T+175 s. Both of these target cases lead to a strength-controlled DART impact, where the increased target strength leads to more pronounced dips in optical depth near the origin at both T+158 s and T+175 s. The dip in  $\tau$  within  $\sim 40$  m of the origin at T+158 s, for the 5 kPa target case, is an observable feature and should have been seen in Figure 2 as a clearing of the plume at low altitude or a plume detachment from Dimorphos. On the other hand, the dip in  $\tau$  near the origin at T+158 s for the 500 Pa target is not an observable feature, as it is barely resolved ( $\sim 3$  pixels in extent), and the plume remains optically thick despite the dip.

At T+175 s in the 500 Pa target case in Figure 8, the optical depth profiles indicate an optically thick plume, meaning  $\tau \gtrsim 1$ ,

out to  $\sim 200$  m from the origin, for both positive and negative  $b$ . This is consistent with the observations of terminators and plume shadows in Figure 4. However, at T+175 s in the 5000 Pa case, the optical depth drops to values  $\tau \lesssim 0.4$ , no longer optically thick, near  $b \approx -200$  m. Hence, the optical depth profiles in the 5000 Pa case are inconsistent with the observations of terminators and plume shadows in Figure 4, which indicate an optically thick plume out to  $\sim 200$  m from the origin.

Thus, the plume optical depth profiles for 5, 50, and 500 Pa are all very similar, with the two-order-of-magnitude increase in target strength leading to less than a factor of 2 decrease in plume optical depth at  $b = \pm 100$  m. However, the further increase in target strength by only one order of magnitude, to 5000 Pa, leads to another factor of 3 decrease in optical depth at  $b = \pm 100$ . This more dramatic decrease in plume optical thickness can be understood from comparing the  $M_{ej}(v)$  curves shown in Figure 6, where the effect of increased target strength on  $M_{ej}(v)$  is seen. Namely, in these strength-controlled cases, the target strength arrests the growth of the crater, so that no more ejecta are released below a cutoff velocity, which is



**Figure 4.** Left: LUKE image acquired at 175 s after DART impact, after closest approach. LICIACube is on departure trajectory. Dimorphos is in front of the ejecta plume. Annotations and scale bar are as in Figure 2. The solar direction is  $6^\circ$  out of the page. The DART incident velocity is directed  $38.2^\circ$  out of the page.

T+175 s

Departure image: Didymos, Dimorphos and ejecta plume

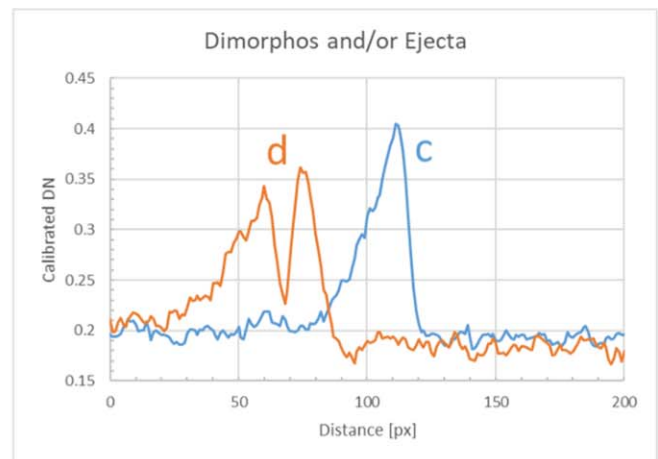
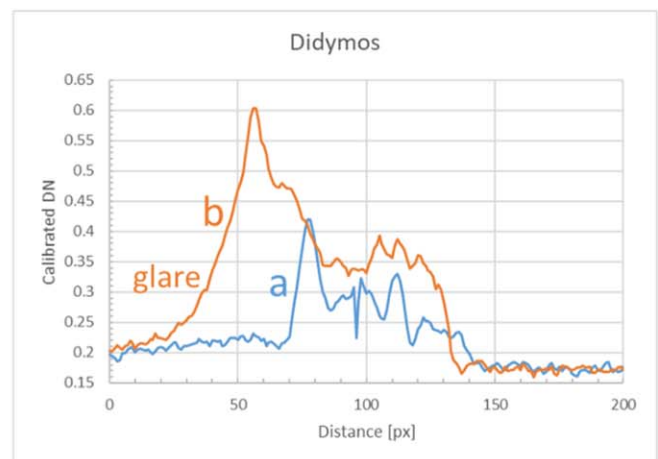
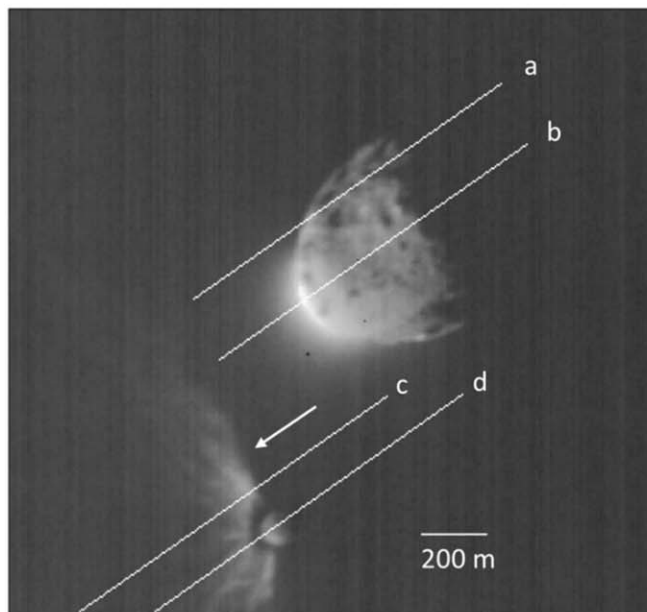


**Figure 5.** Brightness profiles across limbs and terminators of Dimorphos and Didymos, showing DN vs. pixel distance measured from left to right along image lines marked a–d. Profiles a–b are across the terminator and sunlit limb of Didymos, without ejecta plume. Profiles c–d are across the ejecta plume and/or Dimorphos. Dimorphos is in front of the ejecta plume. Profile b below pixel distance 50 shows glare, indicating an excess emission region above the subsolar limb of Didymos. The arrow marks the extent of the sharply defined terminator,  $\sim 200$  km above Dimorphos. The distance 200 m is 34.5 pixels.

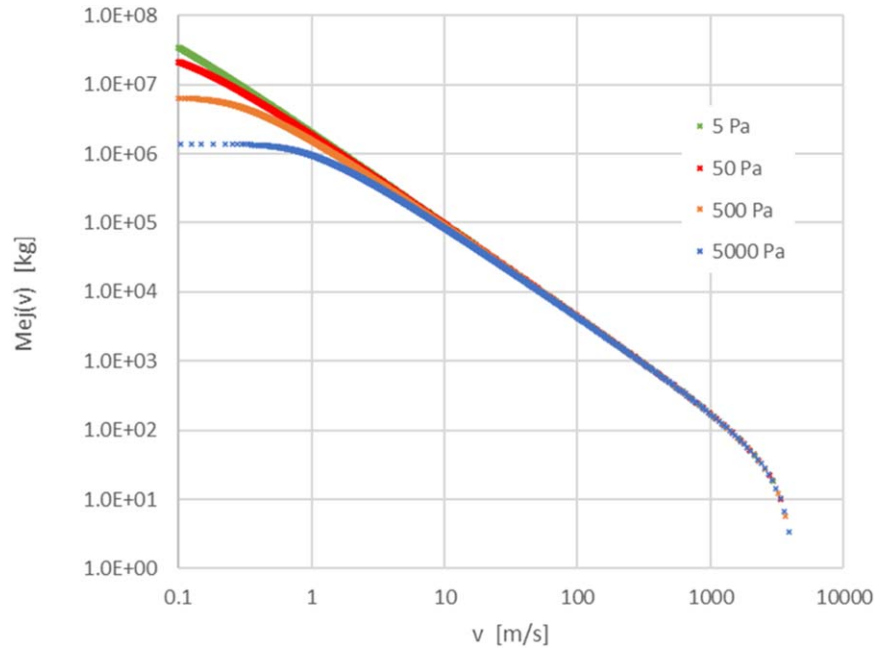


**Figure 6.** Cumulative mass  $M_{ej}(v)$  ejected above velocity  $v$ , for four target cases with strength from 5 Pa to 5 kPa. The ejecta cumulative mass curves for these cases appear in order of increasing strength from top to bottom at the lowest velocities under  $1 \text{ m s}^{-1}$ . That is,  $M_{ej}(v)$  is greatest for the lowest target strength case and least for the highest-strength case. The total ejected mass is similarly greatest for the lowest-strength case.

$\sim 10 \text{ cm s}^{-1}$  at 50 Pa but is  $\sim 1 \text{ m s}^{-1}$  at 5000 Pa. The total ejected mass also decreases for the higher-strength cases (see Table 1). There is about a factor of 5 decrease in total ejected mass going from 5 to 500 Pa, but there is another factor of  $\sim 5$  decrease going from 500 to 5000 Pa.

The predicted crater radius and momentum enhancement factor  $\beta$ , for the DART impact into Dimorphos in the scaling law model with these four target cases, is summarized in Table 1. The crater radius is obtained from Equation (B2), the total ejected mass is the mass  $M_{ej}$  released above  $10 \text{ cm s}^{-1}$ , and  $\beta$  is calculated by numerical integration over the ejecta mass–velocity distribution (Cheng et al. 2016). In the case of 5 Pa target strength, a weak target for which the DART impact is strength controlled, a large crater radius is predicted, large enough that target curvature is important (crater diameter is comparable to target body radius). In this case, the result of the DART impact is not a well-defined crater but a global deformation and reshaping of Dimorphos (Raducan & Jutzi 2022; Raducan et al. 2022, 2024). In the higher-strength cases 50–5000 Pa, a strength-controlled DART impact would lead to a cratering event.

## 5. Discussion and Conclusions

A high momentum enhancement factor  $\beta$  for asteroid deflection by kinetic impact was demonstrated by the DART impact on Dimorphos, where  $\beta$  was found to range from 2.2 to 4.9, scaling with the density for a Dimorphos density range of  $1500\text{--}3300 \text{ kg m}^{-3}$  (Cheng et al. 2023). However, numerical studies have shown that the value of  $\beta$  does not uniquely determine target material properties (like strength or bulk density) or structural properties (like mass fraction of boulders vs. matrix in the interior), but different combinations of these properties can yield the same  $\beta$  for a kinetic impact (Raducan et al. 2019, 2020; Stickle et al. 2022 and references therein). It is important to constrain target material properties and structural properties, in order to understand kinetic impact

processes and to make kinetic impact a reliable mitigation technique for planetary defense.

The DART impact and impact ejecta were monitored by the LICIACube spacecraft, which flew by the Didymos system with closest approach time delayed by 167 s from the DART impact time (Dotto et al. 2021, 2024). Point-source scaling models of the ejecta plume structure and temporal evolution as imaged by LICIACube can be used to constrain target physical properties like strength and porosity (Cheng et al. 2020, 2022). In these models, the ejecta plume structure as it evolves over time is determined by the ejecta mass versus velocity distribution  $M_{ej}(v)$ , which is strongly dependent on target material properties like strength and porosity, making the LICIACube ejecta plume images a powerful diagnostic of the DART impact.

Images of the impact ejecta plume obtained by LICIACube LUKE are compared to models of the ejecta plume optical depth calculated by the method of Cheng et al. (2022), with two significant modifications. The first modification is that DART impact ejecta are described using new point-source scaling relations that are derived from fitting of results from Bern SPH numerical simulations (Raducan et al. 2024; see Appendix B) of the DART impact into rubble pile asteroid models. These numerically derived scaling relations replaced those used in earlier work that were fitted to results of laboratory experiments (Housen & Holsapple 2011). The scaling relations proposed by Cheng et al. (2022) for a gravity-controlled DART impact into a sand target, with strength  $Y = 1 \text{ Pa}$ , predicted  $\beta = 1.62$ , far below the nominal value  $\beta = 3.61^{+0.19}_{-0.25}$  ( $1\sigma$ ) found for the DART impact (Cheng et al. 2023). The second modification to the method of Cheng et al. (2022) is that the plume optical depth model is calculated using a broken power-law ejecta particle size distribution derived from HST observations of the dust tail from the DART impact (Li et al. 2023), replacing the single power-law, Itokawa particle size distribution used in earlier work. The broken



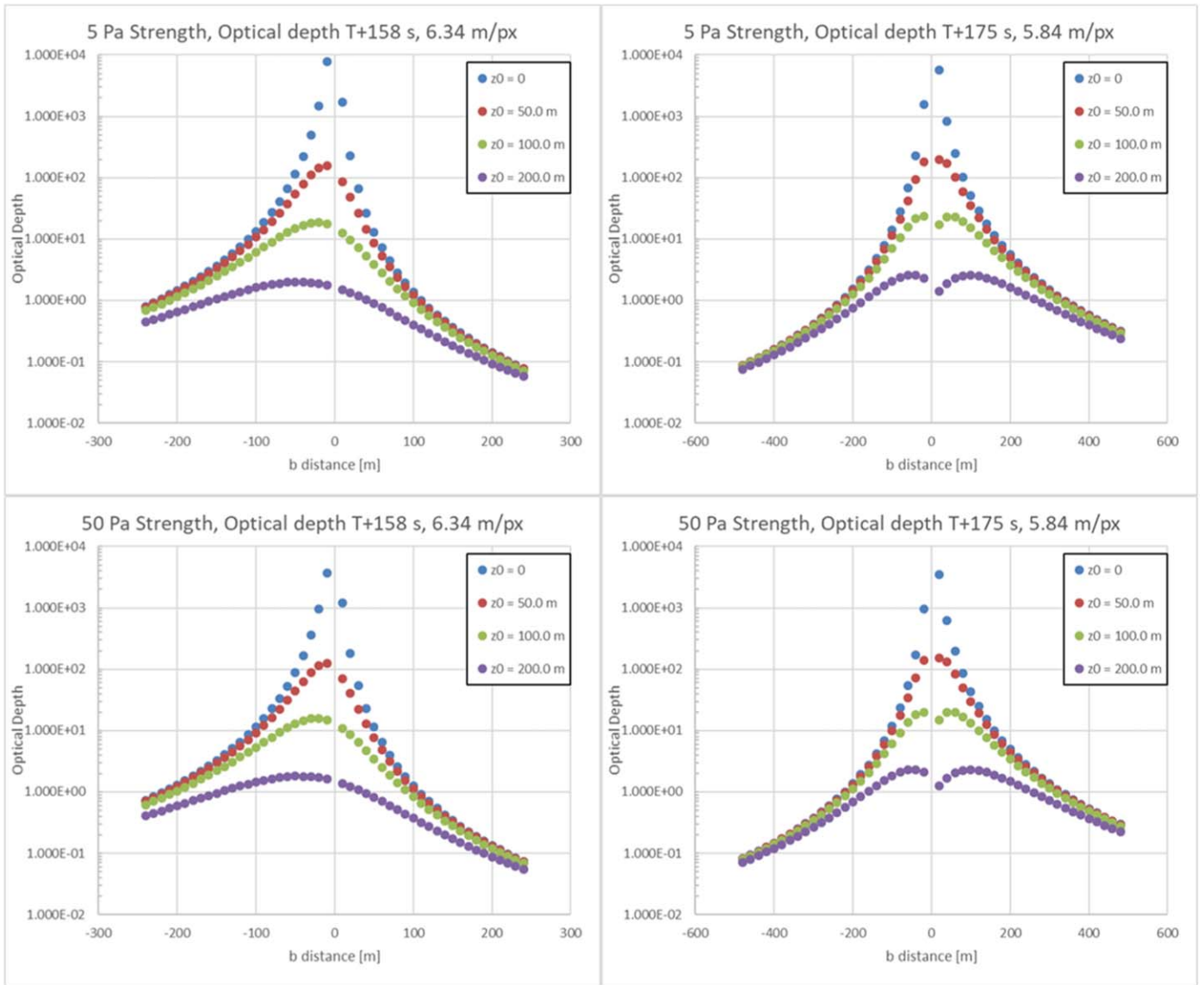


**Figure 7.** Extinction optical depth profiles for 5 and 50 Pa target cases, at image times  $T+158$  s and  $T+175$  s. Image resolutions are indicated. The plume optical depth model is symmetric in  $z$ . Top row: profiles for the 5 Pa case at  $T+158$  s and  $T+175$  s. Bottom row: profiles for the 50 Pa case at the same two times. The peak optical depth value is greatest at  $z_0 = 0$  and takes lower values for larger  $z_0$ .

power-law ejecta size distribution in the present work assumes no velocity dependence of the size distribution.

The point-source scaling models of the impact ejecta plume optical depth evolution are used to distinguish the Dimorphos strength consistent with the high momentum transfer efficiency of the DART impact and with LICIACube ejecta plume imaging. Two of the highest-resolution LICIACube LUKE images of the impact ejecta plume are analyzed in this way, those acquired at  $T+158$  s, 9 s before LICIACube closest approach, and at  $T+175$  s, 8 s after closest approach. The  $T+158$  s image shows no evidence for plume detachment, or clearing of plume opacity at low altitude above Dimorphos. Of the plume optical depth profiles shown in Figures 7 and 8, those at 5, 50, and 500 Pa are consistent with this observation, but the 5000 Pa profiles in Figure 8 are not consistent, due to the sharp decrease in  $\tau$  near the origin. The  $T+175$  s image shows terminators and shadows in the ejecta plume, indicating that the plume is optically thick up to  $\sim 200$  m from Dimorphos. The plume optical depth profiles at 5 and 50 Pa in

Figures 7 and 8 are consistent with this observation, and the 500 Pa profiles are marginally consistent, but the 5000 Pa profile in Figure 8 is not consistent.

On the basis of the LICIACube LUKE imaging of the impact plume, the 5000 Pa target strength case is excluded, but the lower-strength cases at 5, 50, and 500 Pa are not. The same point-source scaling models of the ejecta plume also determine the momentum enhancement factor  $\beta$ , the crater radius, and the total ejected mass, which are shown in Table 1. The  $\beta$  values for the 5 and 50 Pa cases in Table 1 are close to the nominal value  $\beta = 3.61_{-0.25}^{+0.19}$  ( $1\sigma$ ) reported by Cheng et al. (2023), while the  $\beta = 2.74$  in Table 1 for the 500 Pa case would be marginally consistent for a low-density Dimorphos ( $\sim 1700 \text{ kg m}^{-3}$ ). The 5000 Pa case in Table 1 is again excluded because the  $\beta$  value is too low. Consideration of the total ejected mass values in Table 1 leads to a similar conclusion. From ground-based telescopic observations of DART impact ejecta in the visible, Graykowski et al. (2023) estimated a total ejected mass of  $(1.3\text{--}2.2) \times 10^7 \text{ kg}$ . From

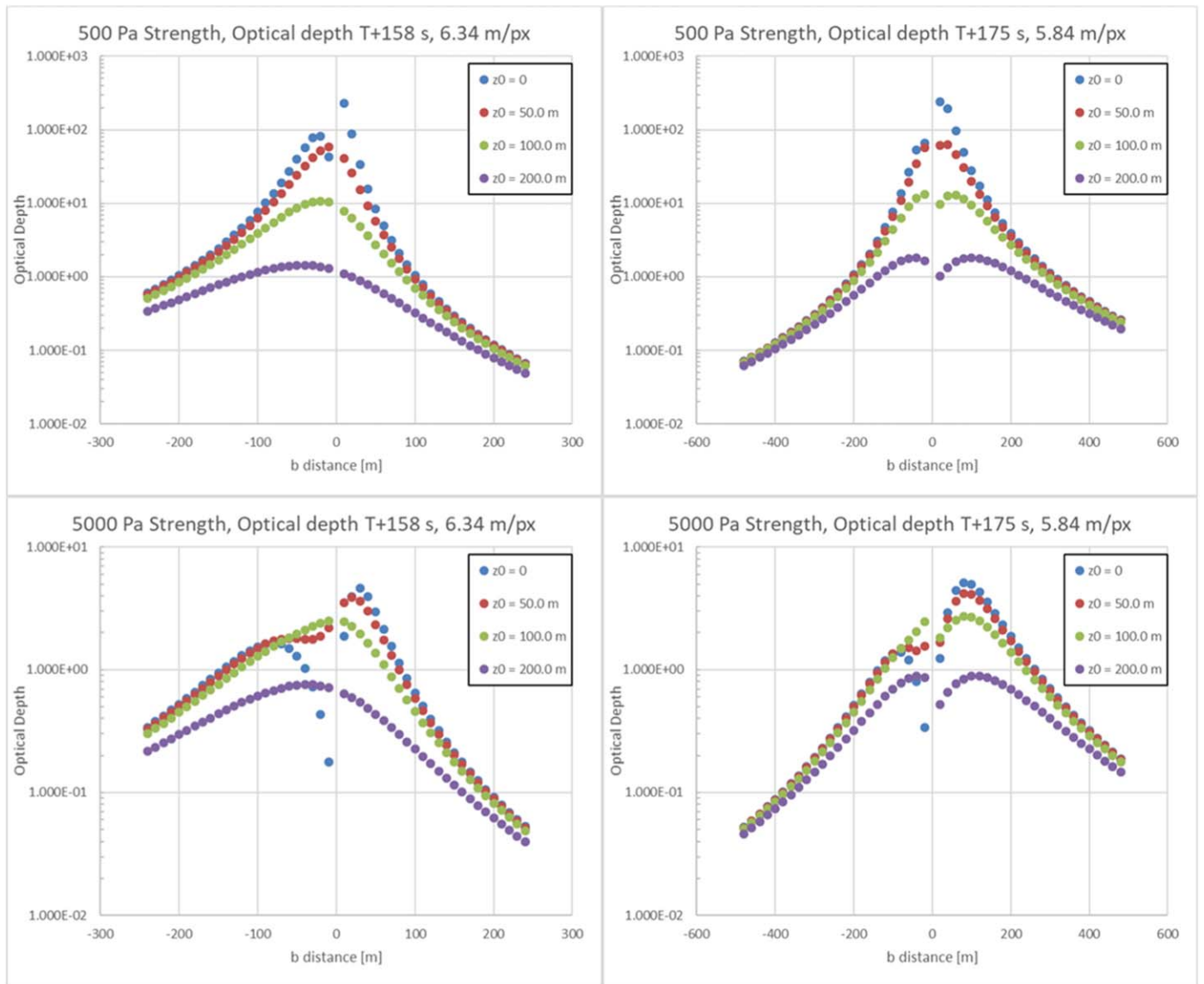


**Figure 8.** Extinction optical depth profiles for 500 and 5000 Pa target cases, at image times  $T+158$  s and  $T+175$  s. Image resolutions are indicated. Top row: profiles for the 500 Pa case at  $T+158$  s and  $T+175$  s. Bottom row: profiles for the 5000 Pa case at  $T+158$  s and  $T+175$  s. The peak optical depth value is greatest at  $z_0 = 0$  and takes lower values for larger  $z_0$ .

**Table 1**  
DART Impact Outcomes from Point-source Scaling

Target Strength $Y$	5 Pa	50 Pa	500 Pa	5000 Pa
Crater radius $R$	40.74 m <sup>a</sup>	24.27 m	14.45 m	8.61 m
Total ejected mass $M_{ej}$	$4.06 \times 10^7$ kg	$2.34 \times 10^7$ kg	$6.48 \times 10^6$ kg	$1.39 \times 10^6$ kg
Momentum enhancement factor $\beta$	3.925	3.444	2.740	2.144

**Note.**

<sup>a</sup> From strength scaling, but global deformation is expected (Raducan & Jutzi 2022).

Atacama Large Millimeter/submillimeter Array millimeter- and submillimeter-wave observations of the DART impact ejecta, Roth et al. (2023) estimated a total ejected mass of  $(0.9\text{--}5.2) \times 10^7$  kg. The total ejected mass  $M_{ej}$  in Table 1 for the 5 and 50 Pa cases is fully consistent with these observational results, while the  $M_{ej}$  for the 500 Pa case is marginally too low, and the  $M_{ej}$  for the 5000 Pa case is an order of magnitude too low and is inconsistent with observations.

In conclusion, the observations of the impact ejecta, including both ground-based observations and LICIAcube in situ observations, and the high momentum transfer efficiency, determined from the orbital period change, are consistent with models of the impact ejecta from the DART impact into a rubble pile Dimorphos, whose impact strength is less than or equal to  $\sim 500$  Pa. The 5 and 50 Pa target cases provide the overall best fit to observations, with similar

predictions for plume optical depth profiles,  $\beta$  and  $M_{ej}$ . However, these cases make dramatically different predictions for crater radius as shown in Table 1. Namely, the 50 Pa target case predicts a crater radius of 24.27 m, while the 5 Pa target case predicts an even larger crater radius, such that a global deformation and reshaping of Dimorphos are expected instead of crater formation (Raducan & Jutzi 2022; Raducan et al. 2022).

The European Space Agency Hera mission will rendezvous with the Didymos system in late 2026 (Michel et al. 2022). Hera will measure the mass of Dimorphos and determine its density, thereby determining  $\beta$  from the DART impact, and it will search for and measure the DART impact crater if it can be identified. In so doing, Hera may infer a Dimorphos strength as low as 10 Pa from the crater radius and morphology formation (Raducan & Jutzi 2022; Raducan et al. 2022). Alternatively, Hera will characterize the reshaping of Dimorphos, possibly determining an even lower strength for Dimorphos, which may be as low as strength  $\lesssim 1$  Pa. In that case, the strength of Dimorphos would be similar to the strengths inferred for asteroids Ryugu (Arakawa et al. 2020) and Bennu (Barnouin et al. 2022; Jutzi et al. 2022; Zhang et al. 2022). Hera may resolve whether the S-type asteroid Dimorphos has similar strength to C-type Ryugu and B-type Bennu, or is significantly stronger.

### Acknowledgments

We thank NASA for support of the DART mission under NASA contract 80MSFC20D0004, and we thank the Italian Space Agency (ASI) for support of the LICIACube project (ASI, contract No. 2019-31-HH.0). S.D.R. thanks the EU Horizon 2020 program, grant 870377. E.D., V.D.C., E.M.E., A.R., I.G., P.J.D.D., P.H.H., I.B., A.Z., S.L.I., J.R.B., G.P., A. L., M.P., G.Z., M.A., A.C., G.C., M.D.O., S.I., G.I., M.L., D. M., P.P., D.P., S.P., P.T., and M.Z. acknowledge financial support from Agenzia Spaziale Italiana (ASI, contract No. 2019-31-HH.0).

### Appendix A Momentum Transfer Efficiency

When a kinetic impactor of mass  $m$  strikes a target at a velocity  $U$ , the momentum transferred to the target of mass  $M$ , written as  $M\Delta v$ , can exceed the incident momentum  $mU$  because of momentum carried away backward by impact ejecta. In general, the vector momentum transfer  $M\Delta v$  is not collinear with the incident momentum vector  $mU$  because the ejecta momentum vector is not antiparallel to the incident direction. The momentum enhancement factor  $\beta$  is defined by the momentum balance of the kinetic impact (Feldhacker et al. 2017)

$$M\Delta v = mU + m(\beta - 1)(\hat{E} \cdot U)\hat{E}, \quad (A1)$$

where the first term on the right-hand side is the incident momentum and the second term is the net momentum of escaping impact ejecta, which is along the unit vector  $\hat{E}$ . This definition of  $\beta$  can be reexpressed as the ratio of the components along  $\hat{E}$  of both the momentum transfer and the

incident momentum vectors, or

$$\beta = \frac{M(\hat{E} \cdot \Delta v)}{m(\hat{E} \cdot U)}. \quad (A2)$$

### Appendix B Point-source Scaling Model of DART Impact

The ejecta plume model is based on point-source impact scaling laws of Housen & Holsapple (2011) as applied by Cheng et al. (2016, 2020, 2022) to the DART impact. A spherical projectile of mass  $m$  and radius  $a$  impacts a half-space target at velocity  $U$  and at normal incidence. The crater radius  $R$  is nondimensionalized by target density  $\rho$  and projectile mass  $m$ , such that the crater radius  $R$ , in the gravity-controlled regime, is

$$R\left(\frac{\rho}{m}\right)^{\frac{1}{3}} = H_1\left(\frac{\rho}{\delta}\right)^{\frac{2+\mu-6\nu}{3(2+\mu)}}\left(\frac{ga}{U^2}\right)^{-\frac{\mu}{2+\mu}} \quad (\text{gravity}), \quad (B1)$$

where the projectile density is  $\delta$ , and where  $\mu$ ,  $\nu$ ,  $H_1$  are dimensionless constant scaling parameters.

In the strength-controlled regime, the crater radius  $R$  is given by

$$R\left(\frac{\rho}{m}\right)^{\frac{1}{3}} = H_2\left(\frac{\rho}{\delta}\right)^{\frac{(1-3\nu)}{3}}\left(\frac{Y}{\rho U^2}\right)^{-\frac{\mu}{2}} \quad (\text{strength}), \quad (B2)$$

where  $Y$  is the target strength. The scaling parameter  $\mu$  depends on target porosity and lies in the range  $1/3 < \mu < 2/3$ , where  $\mu = 1/3$  is the momentum scaling limit and  $\mu = 2/3$  is the energy scaling limit. The scaling parameter  $\nu$  enters via the ratio of target to projectile densities  $\frac{\rho}{\delta}$ , and  $\nu$  is empirically about 0.4 for any target material. The normalization of crater size is given by  $H_1$  or  $H_2$  for gravity or strength scaling, respectively. The transition between the gravity-controlled and strength-controlled regimes occurs where Equations (B1) and (B2) predict the same crater radius.

The ejecta plume mass versus velocity distribution is described following Housen & Holsapple (2011). The cumulative ejecta mass distribution  $M_{ej}(v)$  is given parametrically in terms of the ejecta release radius  $x$  measured horizontally from the impact point in the target surface. The speed of ejecta  $v$  that are released at radial distance  $x$  from the central point of impact, when nondimensionalized by the incident velocity  $U$ , is

$$\frac{v}{U} = C_1\left[\frac{x}{a}\left(\frac{\rho}{\delta}\right)^\nu\right]^{-\frac{1}{\mu}}\left(1 - \frac{x}{n_2 R}\right)^p, \quad (B3)$$

with additional scaling constants  $C_1$  and  $p$ . The mass  $M_{ej}$  ejected from within  $x$ , which is also the mass ejected above the corresponding speed according to Equation (B3), is

$$\frac{M_{ej}}{m} = \frac{3k}{4\pi} \frac{\rho}{\delta} \left[ \left(\frac{x}{a}\right)^3 - n_1^3 \right]. \quad (B4)$$

The ejecta mass versus velocity distribution  $M_{ej}(v)$  is defined implicitly by Equations (B3) and (B4) and has a cutoff at high ejecta velocity, corresponding to the cutoff at small  $x = n_1 a$  in Equation (B4), and additionally a cutoff at low ejecta velocity

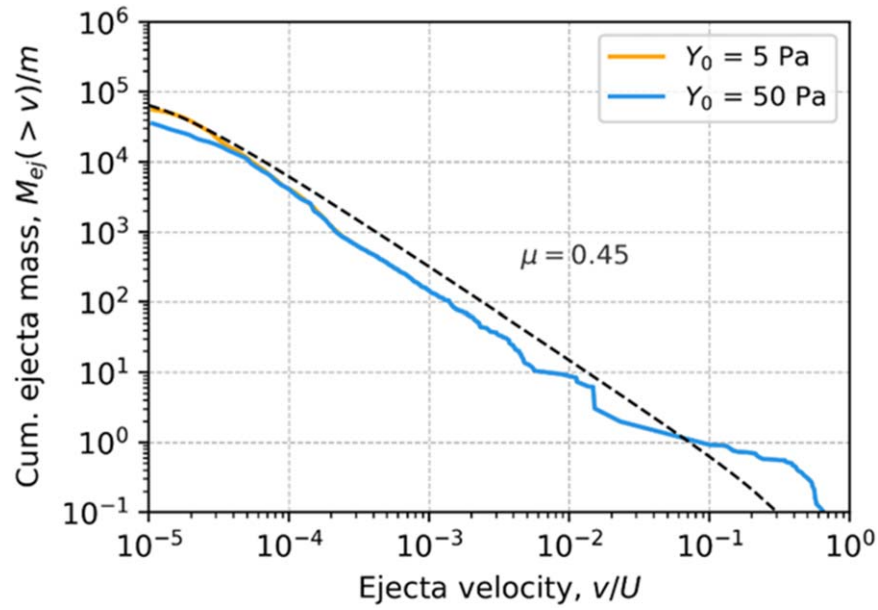


**Figure 9.** Cumulative distributions of ejected mass  $M_{ej}(>v)$  vs. velocity  $v$ , where  $M_{ej}(>v)$  is scaled by projectile mass and  $v$  is scaled by impact velocity. Orange and blue curves show Bern SPH simulations with target cohesion  $Y_0 = 5$  Pa and 50 Pa, respectively. The dashed curve shows point-source scaling relations at cratering strength  $Y = 5$  Pa.

**Table 2**  
Point-source Scaling Parameters for DART Impact Ejecta

$v$	$\mu$	$n_1$	$k$	$H_1$	$H_2$	$n_2$	$C_1$	$p$
0.4	$0.45 \pm 0.02$	0.6	0.42	0.396	0.34	1.3	0.47	0.3

corresponding to large  $x = n_2 R$  from Equation (B3). The scaling parameters  $C_1$  and  $k$  normalize ejecta velocities and ejecta mass, respectively.

Empirical values for the scaling parameters  $\mu$ ,  $\nu$ ,  $H_1$ ,  $H_2$ ,  $C_1$ ,  $k$ , and  $p$  are derived from fitting the scaling relations to ejecta mass and velocity distributions from laboratory experiments (Housen & Holsapple 2011). However, the range of target materials that can be tested in laboratory experiments is limited, and their material properties cannot be varied independently. Numerical simulations can be used to derive the scaling parameters for impact conditions and target material properties for which laboratory experimental results are not available (Priour et al. 2017). Raducan et al. (2019, 2020) used iSALE-2D simulations of the DART impact to derive the scaling parameters for a range of target cases varying the cohesion (shear strength at zero pressure)  $Y$ , coefficients of internal friction  $f$ , and porosity  $\phi$ .

Here we use point-source scaling parameters derived from the shock physics code Bern SPH simulations of the DART impact onto a rubble pile model of Dimorphos (Raducan et al. 2024). These numerical simulations used a fast time integration scheme to describe late-stage evolution, transitioning after passage of the initial shock to modeling a material with low bulk modulus and low sound speed. The projectile for the DART impact model is modeled as a sphere of radius 0.517 m and density  $1000 \text{ kg m}^{-3}$  at mass 579.4 kg of the DART spacecraft, incident on the target at  $6145 \text{ m s}^{-1}$ . The target bulk density is  $2350 \text{ kg m}^{-3}$ . Numerical resolution was such that simulations used  $5.6 \times 10^6$  SPH particles and  $14.5 \times 10^6$  SPH particles. The Tillotson equation of state for basalt was used for the matrix and boulders. The matrix response to shear was treated by a Lundborg

pressure-dependent strength model, with cohesion in the matrix taking values in the range 0–500 Pa. The porosity model was a P- $\alpha$  model. Boulders were explicitly modeled in the SPH simulation down to a size of 2.5 m, and the boulder volume fill fraction was 30%. Boulder tensile strength was 10 MPa. The coefficient of internal friction was  $f = 0.55$ . The strength-gravity transition occurred at  $Y_0 = 4$  Pa.
















The point-source scaling parameters obtained from fitting to the Bern SPH simulations are shown in Table 2. The strength-gravity transition occurs at  $Y = 4$  Pa, the same as for the Bern SPH simulation models.

Figure 9 shows the ejecta cumulative mass versus velocity distribution  $M_{ej}(v)$ , calculated from the point-source scaling parameters of Table 2 with target strength  $Y = 5$  Pa. This distribution was fitted to the distributions  $M_{ej}(v)$  calculated from Bern SPH models of the DART impact with two values for target cohesion,  $Y_0 = 5$  Pa and  $Y_0 = 50$  Pa. The fit in Figure 9 is best fit to the cumulative mass distribution at low velocities up to  $v/U \sim 10^{-4}$ , because the ejecta released at these low velocities are responsible for forming the optically thick plume at low altitude in the images studied in this work. The ejecta released at much higher velocity up to  $v/U \sim 10^{-1}$ , where the fit is off by a factor  $\sim 2$ , are ejecta seen at much higher altitudes or ejecta not seen at all because they are outside the image field of view.

The parameter  $\mu = 0.45 \pm 0.02$  in Table 2 is similar to the value derived by Priour et al. (2017), who found  $\mu \sim 0.43$  for porous targets (porosity  $\sim 30\%$ ) for cratering in the lunar environment. Raducan et al. (2019) derived the same  $\mu$  value for  $\sim 30\%$  porosity for a DART-like impact but with target material properties similar to those assumed by Priour et al. (2017). In addition, the benchmarking study of Luther et al. (2022), comparing fits to the mass-velocity distribution from three different simulations of the DART impact, found  $\mu \sim 0.41$  for  $\sim 30\%$  porosity, which is slightly smaller than the value found by Raducan et al. (2019), as would be expected from the larger coefficient of friction considered by Luther et al. (2022).

The momentum enhancement factors  $\beta$  for the DART impact calculated from the Bern SPH models (Raducan et al. 2024) are as follows: at 5 Pa cohesion,  $\beta = 3.04$ ; at 50 Pa cohesion,  $\beta = 2.72$ . Table 1 shows for comparison the  $\beta$  factors from point-source scaling using the scaling parameters of Table 2: at 5 Pa cohesion,  $\beta = 3.925$ ; at 50 Pa cohesion,  $\beta = 3.444$ . The  $\beta$  from the Bern SPH simulations is about  $\sim 22\%$  lower than the  $\beta$  from the point-source scaling models, which is reasonable considering that the SPH models included target curvature and non-normal incidence angle effects, whereas point-source scaling models did not (Raducan et al. 2024).

### ORCID iDs

Andrew F. Cheng  <https://orcid.org/0000-0001-5375-4250>  
 S. D. Raducan  <https://orcid.org/0000-0002-7478-0148>  
 T. L. Farnham  <https://orcid.org/0000-0002-4767-9861>  
 A. Rossi  <https://orcid.org/0000-0001-9311-2869>  
 P. Hasselmann  <https://orcid.org/0000-0003-1193-8945>  
 S. Ivanovski  <https://orcid.org/0000-0002-8068-7695>  
 J. Brucato  <https://orcid.org/0000-0002-4738-5521>  
 A. Lucchetti  <https://orcid.org/0000-0001-7413-3058>  
 M. Pajola  <https://orcid.org/0000-0002-3144-1277>  
 M. Amoroso  <https://orcid.org/0000-0003-2603-165X>  
 A. Capannolo  <https://orcid.org/0000-0002-4917-287X>  
 M. Dall’Ora  <https://orcid.org/0000-0001-8209-0449>  
 S. Ieva  <https://orcid.org/0000-0001-8694-9038>  
 P. Palumbo  <https://orcid.org/0000-0003-2323-9228>  
 D. Perna  <https://orcid.org/0000-0002-4545-3850>

### References

Arakawa, M., Saiki, T., Wada, K., et al. 2020, *Sci*, 368, 67  
 Barnouin, O. S., Daly, M., Seabrook, J., et al. 2022, *JGRE*, 127, e06927

Cheng, A. F., Agrusa, H., Barbee, B., et al. 2023, *Natur*, 616, 457  
 Cheng, A. F., Michel, P., Jutzi, M., et al. 2016, *P&SS*, 121, 27  
 Cheng, A. F., Raducan, S. D., Fahnestock, E. G., et al. 2022, *PSJ*, 3, 131  
 Cheng, A. F., Stickle, A., Fahnestock, E., et al. 2020, *Icar*, 352, 113989  
 Daly, R. T., Ernst, C. M., Barnouin, O. S., et al. 2023, *Natur*, 616, 443  
 Deshapriya, J. D. P., Hasselmann, P., Gai, I., et al. 2023, *PSJ*, 4, 231  
 Dotto, E., Della Corte, V., Amoroso, M., et al. 2021, *P&SS*, 199, 105185  
 Dotto, E., Deshapriya, J. D. P., Gai, I., et al. 2024, *Natur*, 627, 505  
 Feldhacker, J. D., Bruck Syal, M., Jones, B. A., et al. 2017, *JGCD*, 40, 2417  
 Graykowski, A., Lambert, R., Marchis, F., et al. 2023, *Natur*, 616, 461  
 Güldemeister, N., Wünnemann, K., & Poelchau, M. 2015, in *Large Meteorite Impacts and Planetary Evolution V*, Vol. 518, ed. G. R. Osinski & D. A. Kring (McLean, VA: GSA).  
 Hansen, J. E., & Travis, L. D. 1974, *SSRv*, 16, 527  
 Housen, K. R., & Holsapple, K. A. 2011, *Icar*, 211, 856  
 Jutzi, M., Raducan, S. D., Zhang, Y., Michel, P., & Arakawa, M. 2022, *NatCo*, 13, 7134  
 Li, J.-Y., Hirabayashi, M., Farnham, T., et al. 2023, *Natur*, 616, 452  
 Luther, R., Raducan, S. D., Burger, C., et al. 2022, *PSJ*, 3, 227  
 Mazrouei, S., Daly, M., Barnouin, O., Ernst, C., & DeSouza, I. 2014, *Icar*, 229, 181  
 Mazzotta Epifani, E., Dall’Ora, M., Dotto, E., et al. 2023, *Asteroids, Comets, Meteors Conf.*, 2851, 2388  
 Michel, P., Kueppers, M., Campo Bagatin, A., et al. 2022, *PSJ*, 3, 160  
 Ormö, J., Raducan, S. D., Jutzi, M., et al. 2022, *E&PSL*, 594, 117713  
 Pajola, M., Barnouin, O., Lucchetti, A., et al. 2022, *PSJ*, 3, 210  
 Pajola, M., Tusberty, F., Lucchetti, A., et al. 2023, *LPSC*, 54, 1314  
 Prieur, N. C., Rolf, R., Luther, R., et al. 2017, *JGRE*, 122, 1704  
 Raducan, S. D., Davison, T., Luther, R., & Collins, G. 2019, *Icar*, 329, 282  
 Raducan, S. D., Davison, T. M., & Collins, G. S. 2020, *P&SS*, 180, 104756  
 Raducan, S. D., & Jutzi, M. 2022, *PSJ*, 3, 128  
 Raducan, S. D., Jutzi, M., Cheng, A. F., et al. 2024, *NatAs*, 8, 445  
 Raducan, S. D., Jutzi, M., Zhang, Y., Ormö, J., & Michel, P. 2022, *A&A*, 665, L10  
 Richardson, D., Quinn, T., Stadel, J., & Lake, G. 2000, *Icar*, 143, 45  
 Roth, N. X., Milam, S., Remijan, A., et al. 2023, *PSJ*, 4, 206  
 Stickle, A. M., DeCoster, M., Burger, C., et al. 2022, *PSJ*, 3, 248  
 Tancredi, G., Roland, S., & Bruzzone, S. 2015, *Icar*, 247, 279  
 Thomas, C. A., Naidu, S., Scheirich, P., et al. 2023, *Natur*, 626, 448  
 Zhang, Y., Michel, P., Barnouin, O., et al. 2022, *NatCo*, 13, 4589